

# Lagrangian 3D particle tracking in high-speed flows: Shake-The-Box for multi-pulse systems

Matteo Novara<sup>1</sup> · Daniel Schanz<sup>1</sup> · Nico Reuther<sup>2</sup> · Christian J. Kähler<sup>2</sup> · Andreas Schröder<sup>1</sup>

Received: 10 May 2016 / Revised: 28 June 2016 / Accepted: 14 July 2016 / Published online: 23 July 2016  
© Springer-Verlag Berlin Heidelberg 2016

**Abstract** The Shake-The-Box (STB) particle tracking technique, recently introduced for time-resolved 3D particle image velocimetry (PIV) images, is applied here to data from a multi-pulse investigation of a turbulent boundary layer flow with adverse pressure gradient in air at 36 m/s ( $Re_\tau = 10,650$ ). The multi-pulse acquisition strategy allows for the recording of four-pulse long time-resolved sequences with a time separation of a few microseconds. The experimental setup consists of a dual-imaging system and a dual-double-cavity laser emitting orthogonal polarization directions to separate the four pulses. The STB particle triangulation and tracking strategy is adapted here to cope with the limited amount of realizations available along the time sequence and to take advantage of the ghost track reduction offered by the use of two independent imaging systems. Furthermore, a correction scheme to compensate for camera vibrations is discussed, together with a method to accurately identify the position of the wall within the measurement domain. Results show that approximately 80,000 tracks can be instantaneously reconstructed within the measurement volume, enabling the evaluation of both dense velocity fields, suitable for spatial gradients evaluation, and highly spatially resolved boundary layer profiles. Turbulent boundary layer profiles obtained from ensemble averaging of the STB tracks are compared to results from 2D-PIV and long-range micro particle tracking velocimetry; the comparison shows the capability of the STB

approach in delivering accurate results across a wide range of scales.

## 1 Introduction

During the last decade, tomographic PIV (Elsinga et al. 2006) has become a powerful tool for the investigation of unsteady three-dimensional flows. Its capability to resolve instantaneous 3D flow fields and the complete velocity gradient tensor made it a suitable technique for complex turbulent flow analysis as well as for validation of computational fluid dynamics solutions.

Since its introduction, several methods have been developed aimed at increasing the accuracy and dynamic range of Tomo-PIV measurements. A number of studies focus on the possibility of exploiting time-resolved sequences in order to increase the accuracy of instantaneous recordings (motion tracking enhancement—MTE Novara et al. 2010, sequential MTE—Lynch and Scarano 2015—and fluid trajectory correlation—FTC, Lynch and Scarano 2013). These techniques rely on the tomographic reconstruction of the tracer particles distribution in the 3D domain, followed by 3D cross-correlation of the reconstructed objects to obtain the instantaneous velocity fields.

The spatial resolution of the measurement is limited by the finite size of the cross-correlation volumes. This issue is particularly significant in the presence of strong flow gradients and in proximity of interface surfaces. Several approaches have been presented with the goal of overcoming these limitations (vector reallocation—Theunissen et al. 2008, single-pixel ensemble correlation—Kähler et al. 2006, and adaptive interrogation—Novara et al. 2013). Nevertheless, only particle tracking approaches have been found capable of delivering reliable results in close

✉ Matteo Novara  
matteo.novara@dlr.de

<sup>1</sup> Institute of Aerodynamics and Flow Technology, DLR, Göttingen, Germany

<sup>2</sup> Institute of Fluid Mechanics and Aerodynamics, Bundeswehr University Munich, Neubiberg, Germany

proximity of interfaces and walls (Kähler et al. 2012a) and in strong shear layers (Kähler et al. 2012b).

Three-dimensional particle tracking velocimetry (3D-PTV, Maas et al. 1993) is able to track particles over long trajectories and provide accurate Lagrangian statistics. However, since the accuracy of the PTV particle matching and triangulation algorithm is quite sensitive to overlapping particles (Cierpka et al. 2013a), the seeding concentration is typically reduced by an order of magnitude compared to typical Tomo-PIV experiments (Wieneke 2013).

Recently, the introduction of the iterative particle reconstruction (IPR) technique (Wieneke 2013) opened the possibility for developing particle tracking-based algorithms able to cope with seeding densities typical of that used in tomographic PIV experiments. Being a tracer-particle-based technique, and given its higher precision in terms of particle location when compared to tomographic reconstruction, the IPR represented the ideal starting point for developing a particle tracking algorithm capable of accurately reconstructing long particle trajectories in densely seeded flow (Shake-The-Box, STB—Schanz et al. 2013b, 2016).

The STB method relies on the IPR reconstruction of the initial recordings of a time-resolved sequence; after particle tracks are initialized over a limited number of time instants, it makes use of *particle prediction* from track extrapolation in order to reconstruct and follow tracers at subsequent recordings. After a convergence phase is reached, mainly refinement of the predicted particles position and intensity is needed, as opposed to full IPR triangulation, which largely reduces the computational burden. Furthermore, the STB method implicitly eliminates ghost particles which do not follow coherent trajectories over a long time sequence (Elsinga et al. 2011; Elsinga and Tokgoz 2014).

The performances of STB have been assessed based on both synthetic and experimental time-resolved data (Schanz et al. 2016; Schröder et al. 2015), showing higher accuracy and lower computational time when compared to voxel-based reconstruction and correlation techniques.

When compared to standard double-frame PIV, the availability of particle tracks allows, on the one hand, to increase the accuracy of the velocity estimate through high-order polynomial fitting of the particle position in time, which further reduces the position error of the reconstruction technique. Furthermore, effects due to acceleration and curvature can be eliminated (Scharnowski and Kähler 2013; Cierpka et al. 2013a). On the other hand, the material acceleration can be derived from the fitted tracks, which can be used in combination with the Navier–Stokes equations to obtain instantaneous 3D pressure fields (van Oudheusden 2013; Huhn et al. 2015).

Due to actual hardware limitations in terms of maximum acquisition frequency, time-resolved sequences suitable for

particle tracking can be obtained only in low-speed flows, typically slower than 10 m/s.

When dealing with larger flow velocities, typical of industrial and aerodynamics applications, dual-frame PIV systems are typically employed where the recording of two pulses in rapid succession ( $\Delta t$  of a few microseconds) is followed by a large time interval (typically a few milliseconds) before a new couple of realizations can be acquired.

A two-pulse Tomo-PTV method has been proposed by Cornic et al. (2014) based on the concept of sparse tomographic reconstruction (LocM-CoSaMP, Cornic et al. 2013), where particles in the 3D domain are matched between the two pulses in order to evaluate the displacement field.

In order to increase the measurement dynamic range, multi-pulse approaches have been proposed that make use of multiple tomographic imaging and illumination systems. Synchronizing the acquisition of two dual-frame systems in a staggered fashion makes it possible to obtain short four-pulse time-resolved sequences, where the time separation can be freely reduced down to a few microseconds. This approach has the advantage that the light intensity is completely independent of the pulse frequency in contrast to what happens with high-repetition rate lasers.

Recently, 3D PIV multi-pulse investigations were successfully conducted in air at 10–20 m/s; the data were processed by means of voxel-based tomographic reconstruction and correlation techniques (Schröder et al. 2013; Lynch and Scarano 2014).

In the present study, the STB method is applied to multi-pulse data of a turbulent boundary layer in air at 36 m/s. The aim of the study is to provide dense fields of accurate Lagrangian particle tracks which can be used to obtain high spatial resolution flow statistics and dense data for the evaluation of spatial flow gradients, avoiding the signal modulation introduced by cross-correlation windowing approaches.

The lack of a long sequence of time-resolved recordings makes it necessary to adapt the STB strategy proposed by Schanz et al. (2013b) into an iterative process able to cope with the relatively high particle image density; this aspect is discussed in the remainder of the paper. A correction scheme is proposed to compensate for structural vibrations resulting in camera displacement; also, a method to accurately identify the wall location within the measurement domain is presented.

Results are shown in terms of instantaneous tracked particle fields; the FlowFit technique (Gesemann 2016) is used to interpolate the scattered results obtained from the particle tracks to a regular Cartesian grid for the visualization of instantaneous vortical structures. An ensemble averaging approach is used to obtain flow statistics in terms of

boundary layer profiles; the comparison of the results with those obtained with 2D-PIV and long-range micro-PTV is discussed.

## 2 Multi-pulse acquisition strategy

When time delays of a few microseconds ( $\Delta t < 50 \mu\text{s}$ ) are required to follow the particle image motion reliably, a combination of multiple double-pulse systems can be employed to overcome the intensity and frequency limitations of current high-repetition rate laser systems. In the present study, two independent lasers each with double-pulse capabilities (BigSky Ultra 400) are used to generate four independent pulses with desired time delay.

To separate the particle images from the subsequent pulses, different strategies have been adopted. Lynch and Scarano (2014) proposed the use of three independent tomographic recording systems ( $S$ ), the first two operating in single-frame mode to capture the two initial laser pulses ( $L_1$  and  $L_2$ ) and the third operating in double-frame mode with  $L_3$  and  $L_4$ . The use of single-frame mode is motivated by the long exposure time (several milliseconds) of the second frame in double-shutter mode due to the readout time. As this strategy requires the use of a large number of cameras (at least nine), a sufficient optical access to the test section is needed. Moreover, as explained in detail in the remainder of the study, the use of three independent imaging systems is not suitable for the a posteriori identification and correction of camera shifts caused by structural vibrations.

In order to overcome these limitations, often encountered when operating in large industrial facilities, an approach based on the use of polarized light has been proposed (Kähler and Kompenhans 2000; Schröder et al. 2013) and it is followed in the present study (Fig. 1).

Two independent lasers emit two pulses separated by a  $\Delta t$  of  $20 \mu\text{s}$ , effectively providing four pulses with a time separation of  $10 \mu\text{s}$ . Two imaging systems are operated in double-frame mode; in order to separate the particle images from different pulses, cameras are equipped with polarizing filters rotated by  $90^\circ$  with respect to each other.

The polarization-based approach requires particles to be spherical in order to maintain the polarization direction of the scattered light. Furthermore, the angle between the cameras and the polarization axes needs to be lower than  $20^\circ$  in order to preserve the extinction rate of the polarizers and avoid multi-exposed images (Schröder et al. 2013). On the other hand, with respect to the method proposed by Lynch and Scarano (2014), only two independent imaging systems are employed, which largely reduces the complexity of the setup and offers a more practical solution in case of limited optical access.

Furthermore, when structural vibrations result in camera displacement with respect to their calibrated positions, a situation commonly encountered in industrial facilities, a method for identifying and compensating for the spurious particle displacement induced by the camera movement can be adopted. The vibration correction strategy is described in the remainder of the study.

Recently, frame-optimized exposure cameras (FOX, Geisler 2014) have been developed, which allow for the acquisition of two frames with short exposure time (with reduced resolution along one direction) and of a third frame in full resolution. As a consequence, when FOX cameras are adopted for the first imaging system, a pulse separation strategy based on temporal multiplexing can be implemented (Fig. 2), avoiding the potential imaging issues of the polarization-based approach. Furthermore, the third frame from the FOX cameras can be used to acquire the fourth pulse, therefore offering a direct solution to solve the problem of vibration-induced displacement between the

**Fig. 1** Pulse separation timing diagram for multi-pulse acquisition with polarization-based strategy. Red and blue color refer to the polarization directions of laser 1 and 2, respectively

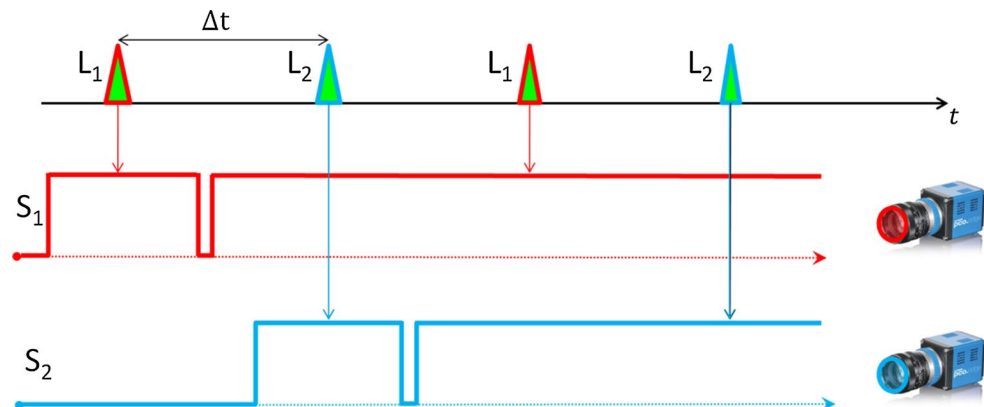
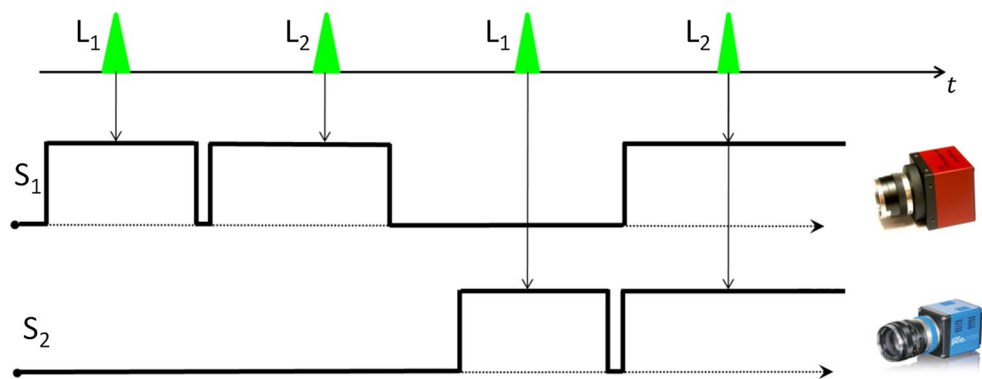


**Fig. 2** Pulse separation based on timing using frame-optimized exposure (FOX) cameras for  $S_1$



two imaging systems. The investigation of the latter pulse separation strategy goes beyond the scope of the present study and it is devoted to a future work.

### 3 Shake-The-Box for multi-pulse recordings

The Shake-The-Box method (Schanz et al. 2013b, 2016) is a 3D particle tracking technique aimed to the accurate reconstruction of long particle tracks. The method is based on the iterative particle reconstruction technique (IPR, Wieneke 2013); unlike for MART (multiplicative algebraic reconstruction technique, Herman and Lent 1976)-based approaches commonly used in Tomo-PIV, IPR does not rely on the discretization of the 3D domain into voxel elements; particles are represented only by the peak location and intensity, which largely reduces the computational burden of the reconstruction. The IPR performances in term of particle position accuracy exceed those of MART-based algorithm in a wide range of seeding densities, up to 0.05 *ppp* (particles per pixel).

The STB technique has been proposed for the evaluation of time-resolved data, where the long observation time can be exploited to enhance the accuracy of the single realizations. With respect to previously proposed methods, such as the MTE and the FTC, the novel concept of *particle prediction* has been introduced within the framework of the STB.

When particle tracks have been initialized across an initial number of recordings reconstructed with full IPR processing (typically 4–5), the tracked particle locations at a subsequent instant can be estimated from the extrapolation of the available tracks. The estimated particle position is then corrected by means of the image matching step of the IPR method (*particle shaking*); the computational cost is reported to be a factor 5–20 lower compared to Tomo-PIV processing, depending on the volume depth and the number of particles (Schanz et al. 2016). A recent application of the *particle prediction* approach has been proposed by Lynch and Scarano (2015) to further extend the capabilities of the MTE technique.

Combining the particle location accuracy of IPR with the exploitation of the temporal information from the time-resolved sequence of recordings allows STB to cope with higher seeding density than previously possible for MART and IPR alone and exceed the limit of 0.05 *ppp*.

Tracked particles are predicted, *shaken* to their corrected position and subsequently back-projected onto the image plane to form *projected images* ( $I_{\text{proj}}$ ) as:

$$I_{\text{proj}}^i = \sum_p I_{\text{part}}^i \quad (1)$$

where  $i$  loops over the cameras in the imaging system and  $p$  over the number of triangulated particles. The *particle reprojected image* ( $I_{\text{part}}$ ) is generated for each 3D particle making use of the optical transfer function obtained by a parametrization of the particle image shape during volume self-calibration (OTF, Schanz et al. 2013a). The *projected images* are subtracted from the original recorded images ( $I_{\text{orig}}$ ) to obtain the *residual images* ( $I_{\text{res}}$ ) as:

$$I_{\text{res}}^i = I_{\text{orig}}^i - I_{\text{proj}}^i \quad (2)$$

The *residual images*, exhibiting a lower imaged seeding density, are processed with further IPR iterations in order to reconstruct previously not tracked particles. The number of successfully tracked particles progressively increases as the STB works its way along the recording sequence, reaching a converged state after a number of time instants depending mainly on seeding density and image quality (typically 4–20 recordings are required, Schanz et al. 2016).

When compared to 3D-PTV (Maas et al. 1993), typically limited to 0.005 *ppp*, STB offers the possibility of a dense representation of the velocity field which allows for the investigation of instantaneous flow structures and spatial gradients, avoiding the signal modulation typically introduced by cross-correlation-based approaches. This makes the STB a suitable technique for the investigation of turbulent flows where strong gradients and a wide range of spatiotemporal scales are present, but also wall-bounded flows where the large gradients appearing in the near-wall region can be reliably resolved without any

bias error due to spatial smoothing. Moreover, the availability of long particle tracks also grants access to particle acceleration which can be used in combination with the momentum equation to extract the 3D pressure distribution with non-intrusive PIV investigations (van Oudheusden 2013; Huhn et al. 2015).

For details regarding the IPR and STB processing parameters and performances, the authors refer to Wieneke (2013) and Schanz et al. (2016), respectively.

When a multi-pulse acquisition strategy is considered by combining different lasers, a long recording sequence is not available. The consequence of the limitations provided by the four time-resolved pulses is twofold. On the one hand, *particle prediction* cannot be used as the image sequence is limited to four frames, which is the typical number of recordings used for track initialization. This reduces the capabilities of the technique to cope with high seeding densities as the IPR reconstruction has to deal with the full recorded images instead of the less complex problem offered by the processing of *residual images*.

On the other hand, the likelihood of ghost particles being coherent with the flow motion along a short four-pulse recording sequence is increased with respect to the fully time-resolved case, where the STB result can be considered almost as *ghost free* (Schanz et al. 2016). The presence of ghost tracks introduces modulation of the velocity

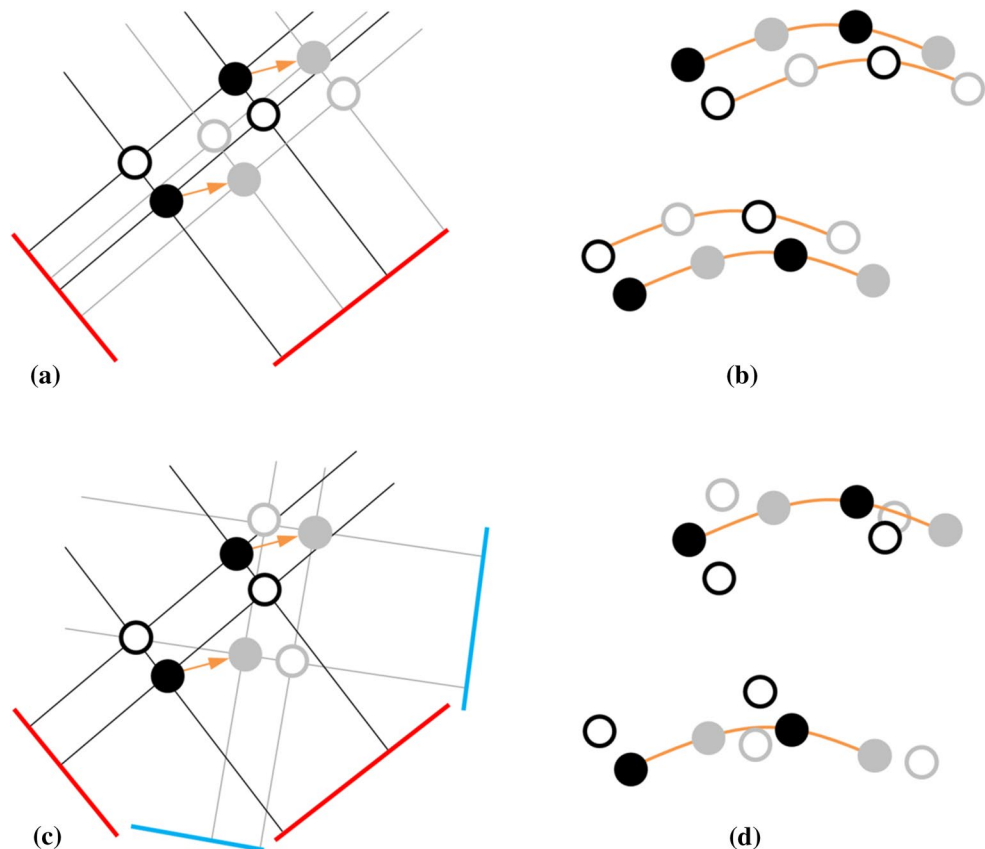
gradients affecting the spatial resolution of the measurement (Elsinga et al. 2011).

A novel iterative approach for STB is proposed in the present study aiming to overcome the aforementioned issues related to the limited time information available for multi-pulse investigations. The use of two independent viewing systems imaging the same particles along the four time instants largely reduces the chances of coherent ghost particles tracks. The iterative application of IPR and particle tracks identification appears to be effective in coping with higher seeding density than what is possible by means of IPR alone.

### 3.1 Particle tracking with independent imaging systems

While in the case of time-resolved data STB relies on the long observation time to avoid the onset of ghost tracks, in the present study the key to a ghostless reconstruction is aided by the use of two independent imaging systems. Since the location of the ghost particles depends on the relative position between the cameras and the actual particles, the use of two different sets of cameras—having different viewing directions with respect to the particles—results in ghost peaks incoherent with the flow velocity field (Discetti et al. 2013).

**Fig. 3** Sketch of actual (*full*) and ghost (*hollow*) particles reconstruction for single (**a, b**) and dual tomographic system (**c, d**). **a, c** Two reconstructed subsequent exposures (*black* and *gray*); *orange vectors* indicate the true particle displacement field. **b, d** Reconstructed tracked particles over four time instants (*black* for  $t_{1,3}$ , *gray* for  $t_{2,4}$ )





This principle is shown in Fig. 3 with reduced dimensionality for the sake of clarity. The reconstruction of two particles at two subsequent time instants from a two-camera system is shown in Fig. 3a; ghost particles are formed at the intersection of lines-of-sight corresponding to active pixels.

When the actual particles experience a uniform displacement, the resulting ghost particles will be coherent with the flow motion; in case of a sequence of recordings, Fig. 3b, *ghost tracks* are formed. On the other hand, when two independent systems are employed, Fig. 3c, the different geometry of the lines-of-sight pattern results in completely uncorrelated ghost particles which do not produce coherent tracks along the four recordings, Fig. 3d.

### 3.2 Iterative STB implementation

The principle illustrated in Fig. 3 is exploited within the iterative STB processing approach proposed in the present study, Fig. 4. The recorded images ( $I_{orig}$ ) are reconstructed via IPR to triangulate and correct (*shake*) particles for each of the four pulses; within the IPR processing the number of triangulations ( $m$ ), triangulation with one camera missing ( $n$ ) and shaking iterations ( $k$ ) can be chosen based on the image quality and seeding density. After the second recording ( $t_2$ ) is reconstructed, a partner search between the reconstructed particle fields is performed in order to build potential tracks (*track candidates*). For each particle  $p$  found at time  $t_2$ , a search area  $A_r$  is centered at the particle location  $\vec{x}_{p,t_2}$ . If a predictor for the velocity field ( $\vec{u}_{pred}$ ) is available (e.g., average field from PIV), the center of the search area is positioned based on the estimated particle displacement within the time interval between the two recordings ( $\Delta t$ ) as:

$$\vec{x}_{A_r,t_1} = \vec{x}_{p,t_2} - \vec{u}_{pred} \cdot \Delta t \tag{3}$$

If a predictor field is not available, the choice of the search area radius  $r$  depends on the magnitude of the estimated particle displacement. Within this search area, all

particles at time  $t_1$  are found and, for each of these particles, a track candidate is built. The same is done at the following time steps, building new *track candidates* connecting particles between  $t_2$  and  $t_3$  and so on. Furthermore, when one or more *track candidates* are found within the search area at the previous time step, the potential tracks are extended by adding the particle at the current time instant.

After the last pulse is reconstructed and the evaluation of the *track candidates* completed, a first degree polynomial is used to fit the particle position along the track and the average deviation of the particles from the fit is computed as:

$$\varepsilon_{fit} = \left| \frac{1}{N} \sum_{i=1}^N \sqrt{(\vec{x}_{i,p} - \vec{x}_{i,fit})^2} \right| \tag{4}$$

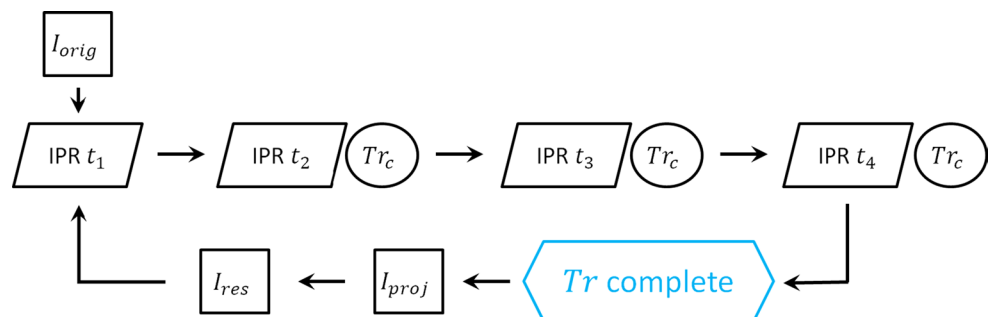
where  $\vec{x}_{i,p}$  indicates the reconstructed particle location at each time instant,  $\vec{x}_{i,fit}$  the location resulting from the polynomial fit and  $N$  equals the number of pulses. Among the track candidates that have one or more particles in common, the one with the lowest value of  $\varepsilon_{fit}$  is chosen, while the others are discarded. If the deviation of the chosen track candidate is smaller than a threshold value  $T_{\Delta f}$  (typically  $1-2px$ ), the track candidate is considered as a valid track.

Among all the identified tracks, only the ones having length equal to the number of pulses are retained at the  $Tr_{complete}$  step; based on the considerations made in the previous section, this step is expected to exclude potential ghost tracks and retain only actual particles. After  $Tr_{complete}$  is performed, retained particles are back-projected for each time instant to obtain projected ( $I_{proj}$ ) and residual ( $I_{res}$ ) images as indicated in Eqs. 1 and 2.

These steps constitute a single STB iteration; depending on the chosen parameters for IPR (intensity imaged particle peak threshold  $T_{int}$ , number of triangulations and shaking iterations, allowed triangulation error  $\varepsilon$ ) and for the track identification (search radius, smoothness threshold  $T_{\Delta f}$ ), only a portion of the actual particles are successfully tracked after the first STB iteration.

Actual particles which have not been tracked result in particle images within the *residual images*; performing

**Fig. 4** Sketch of iterative STB processing for multi-pulse sequences



further STB iterations starting from the *residual images* allows for the reconstruction and tracking of particles that have not been tracked in the first iteration (e.g., due to overlapping particle), thus enabling the technique to deal with seeding density that cannot be successfully reconstructed by using the IPR reconstruction alone.

In this respect, the iterative approach represents for the multi-pulse case what the exploitation of a long observation time is for time-resolved STB where, within the convergence phase, only particles that have not been previously tracked are introduced by the triangulation of following recordings.

The iterative STB processing technique is applied here to multi-pulse data from an experimental investigation of a turbulent boundary layer in air in the presence of an adverse pressure gradient. The description of the experimental

setup and of the processing parameters is given in the following sections.

## 4 Experimental setup

The experiment is conducted in the large-scale atmospheric wind tunnel Munich (AWM) at the Bundeswehr University (Munich, Germany). The closed test section of the open circuit facility is 22 m long and has a cross-sectional area of  $1.8 \times 1.8 \text{ m}^2$ . The free-stream velocity in the test section ranges from 2 to 45 m/s; results relative to a free-stream velocity of 36 m/s are shown in the present study.

The model shown in the sketch in Fig. 5 is located at the vertical wall of the test section in order to produce an

**Fig. 5** Two views of the wind tunnel model; flow direction aligned with  $X$  axis. **a** *Yellow circle* indicates the location of the glass window used as optical access point for the tomographic imaging system. **b** *Green rectangle* indicates the location of the 3D measurement domain

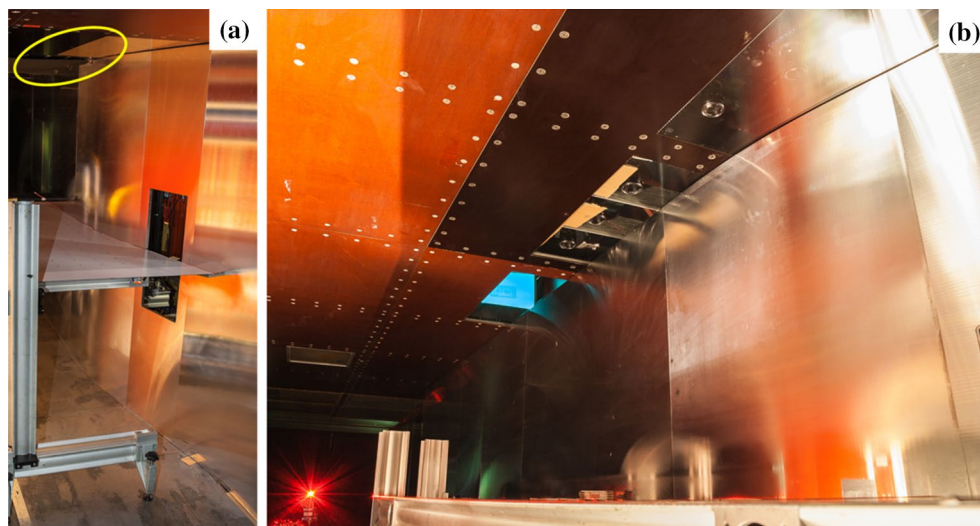
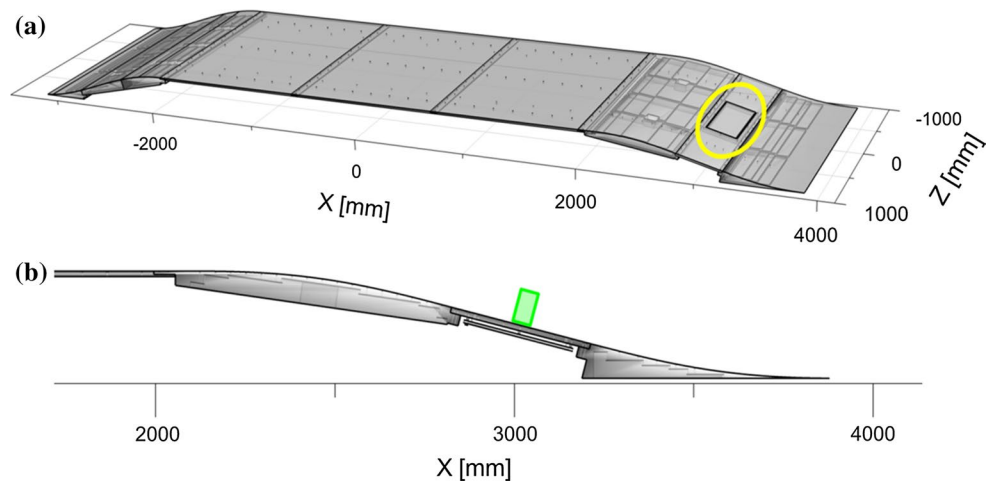


**Fig. 6** **a** Model installed at the vertical wall of the test section (on the right side in the picture); the glass window providing optical access for the 3D imaging system is located at the center of the model along the span-wise direction. The target plate used to calibrate the planar

PIV system is placed perpendicular to the model surface. **b** Detail of the ceiling of the test section within the region indicated by the *yellow circle* in **a**; glass windows allow optical access for the multiple planar PIV and long-range micro-PIV imaging systems

adverse pressure gradient within the turbulent boundary layer; the model is approximately 7 m long and encompasses the whole height of the test section, Fig. 6a. A multi-planar large-scale PIV system consisting of nine sCMOS PIV cameras is placed on top of the test section, Fig. 6b, in order to measure the whole extension of the boundary layer over approximately 2.3 m in stream-wise direction, including the region of the model glass window (indicated with a yellow circle in Fig. 5), where the 3D measurement is located. Moreover, a long-range micro-PIV system is used to investigate the near-wall region located within the same measurement domain of the tomographic system. For details about the 2D-PIV and long-range micro-PIV experimental setups, the authors refer to Reuther et al. (2015).

The 3D measurement domain is located approximately at the center of the glass window along the  $X$  direction and at 910 mm from the test section floor. The measurement volume extends for 90 mm normal to the glass wall ( $Y$  direction) and encompasses 50 mm along the stream-wise ( $X$  direction); the thickness of the illuminated area extends for approximately 8 mm along the span-wise  $Z$  axis.

For the results presented in the following sections, the origin of the coordinate system is located 136.2 mm downstream of the upstream edge of the glass window along  $X$ , at 910 mm from the wind tunnel floor ( $Z$ ), and at approximately 53 mm from the glass wall ( $Y$ ).

The two imaging systems Fig. 7a, consist of four PCO Edge scientific-CMOS cameras each; the sensor size is  $2560 \times 2160$  px and the pixel size  $6.5 \mu\text{m}$ . Cameras, in Scheimpflug condition, are equipped with Zeiss objectives having a focal length  $f = 100$  mm; the focal number  $f_{\#}$  is set to 8. The digital resolution is approximately  $35 \text{ px/mm}$ .

Illumination is provided by a pair of double-cavity laser systems BigSky Ultra 400. The independent laser systems with orthogonal polarization state are combined on the same optical axis using dichroic mirrors, and superimposed beams are expanded to illuminate the 8 mm thick measurement domain (the example shown in Fig. 7b refers to a different system consisting of two Innolas Spitlight 1000, where the combination of the laser beams happens externally to the casing). The laser access is granted by an optical window on the opposite side of the test section with respect to the location of the model glass window. The flow is seeded with DEHS (Di-Ethyl-Hexyl-Sebacate) droplets of approximately  $1 \mu\text{m}$  in diameter; the spherical shape of the particles and the limited angle between the cameras and the  $XY$  plane of the measurement domain are aimed at reducing the risk of depolarization of the scattered particle light. The seeding density varies between 0.03 and 0.04 particles per pixel ( $ppp$ ).

The calibration of the imaging system is carried out using a two-plane 3D target plate simultaneously imaged by all eight cameras. Volume self-calibration correction (VSC, Wieneke 2008) is applied in order to reduce the calibration errors. The self-calibration step is performed making use of images recorded at low seeding density where the tomographic systems record simultaneously, as the same particle images are needed to detect the disparity error. Moreover, this step allows for the evaluation of the optical transfer function (OTF), particularly important for the iterative particle reconstruction technique step within the STB processing. A further VSC iteration is performed independently for the two systems making use of the actual measurement images.

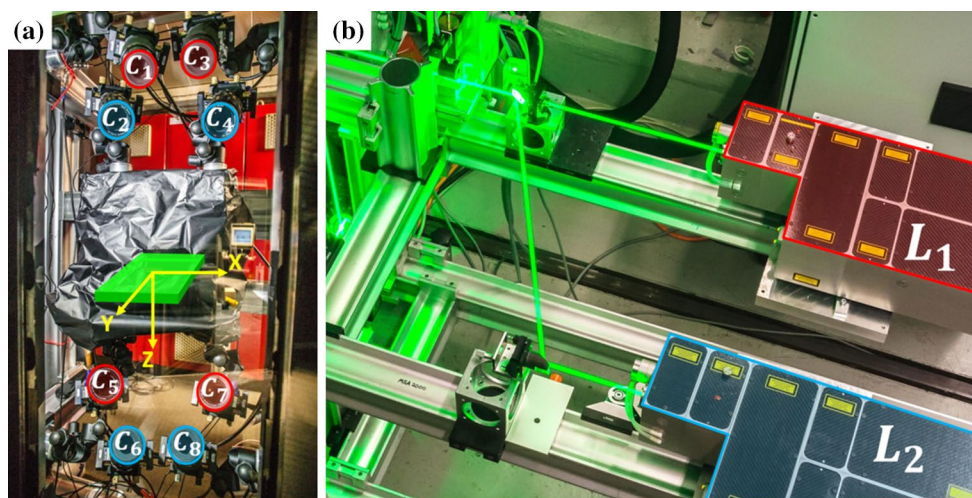


**Fig. 7** **a** View of the two tomographic systems (cameras 1/3/5/7 and 2/4/6/8) from inside the test section; sketch of the illuminated region, in green (not to scale), and reference system in yellow

**b** Example of dual illumination system (Innolas Spitlight 1000); lasers combined onto the same optical axes



The geometrical arrangement of the two systems is symmetric in order to achieve comparable uncertainties of the particle location reconstruction. All cameras are in forward-scattering condition to enhance the signal strength.

Results shown in the remainder refer to a configuration where the  $\Delta t$  between subsequent pulses is kept constant at 10  $\mu\text{s}$  (30  $\mu\text{s}$  between the first and last pulse). Nevertheless, the setup allows to freely choosing the time separation, also in an unevenly spaced manner; the latter solution could be used to increase the velocity and acceleration dynamic range and is not explored in the present study.

With the chosen time separation, the maximum particle displacement between subsequent pulses is approximately 15 px. A sequence of 20,000 recordings is recorded with a frequency of 10 Hz; for each recording, a four-pulse time-resolved sequence is available.

## 5 Application of STB

The iterative STB processing technique is applied to the multi-pulse images; the processing parameters employed to obtain the results shown in the following are summarized in Table 1. The reconstruction and tracking parameters are chosen based on the available literature relative to the application of IPR and STB both to synthetic and experimental data (Wieneke 2013; Schanz et al. 2016); a final tuning of the parameter is performed based on the visual inspection of the residual images and track results.

Before performing STB, images are pre-processed subtracting from each pixel the minimum intensity value along the complete recording sequence, with the aim of reducing the stationary high-intensity reflections caused by the laser light impinging on imperfections within the window glass.

**Table 1** Processing parameters for the iterative Shake-The-Box;  $N_c$  indicates the number of cameras in each imaging systems

Parameter	Process	Value
Triangulation iterations with $N_c$	IPR	$m = 2$
Triangulation iterations with $N_c - 1$	IPR	$n = 1$
Shake iterations	IPR	$k = 5$
Shake width	IPR	$\delta_s = 0.1$
Allowed triangulation error (px)	IPR	$\varepsilon = 1.1$
Intensity threshold (counts)	IPR	$T_{\text{int}} = 150$
Proj. factor prior to triangulation	IPR	2
Predictor field	Tracking	Avg. Tomo-PIV field
Search radius (from velocity predictor) (px)	Tracking	6
Smoothness threshold (px)	Tracking	$T_{\Delta f} = 2$
STB iterations	STB	5

The track identification step is performed with the aid of a predictor velocity field from Tomo-PIV. An in-house implementation of sMART (Atkinson and Soria 2009) is performed to reconstruct  $1700 \times 3200 \times 250 \text{ vox}^3$  objects; LaVision Davis 8.2 is employed to perform direct cross-correlation of the reconstructed objects and obtain velocity vector fields. The computation is performed on a twenty cores server equipped with two Xeon E5-2680 quad core CPUs; the computational time needed to obtain a single velocity field is of approximately 14 min (reconstruction and cross-correlation of two pulses). Due to the significant computational cost, the use of instantaneous velocity predictors is unpractical; 50 recordings only are processed with Tomo-PIV, and an average velocity field is evaluated to be used as a predictor to aid the tracking process.

Recently, the particle space correlation approach has been introduced (PSC, Novara et al. 2016) which allows the evaluation of velocity vector fields on a regular grid directly from particle distributions as obtained from particle based reconstruction techniques (e.g. IPR) or object-oriented approaches (Ben Salah et al. 2015). Particles are represented only by their position and intensity and the method does not rely on the discretization of the complete domain in voxel elements. Furthermore, when the STB processing is considered, the IPR reconstruction of the four pulses is already available and no extra processing is required. Based on the results shown in Novara et al. (2016), the application of the PSC technique could enable the use of instantaneous velocity field predictor within the STB processing strategy.

The number of tracks identified after each STB iteration is shown in Fig. 8b for three recordings along the acquisition sequence. As expected, the number of tracks increases with the number of iterations, eventually reaching an asymptote; for most time instants, 3–4 iterations seem to be sufficient.

The dashed line in Fig. 8a shows the result relative to the first recording where a single STB iteration is performed increasing the number of triangulations and *shaking* steps ( $m = 8, n = 7, k = 10$ ); the fact that no significant increase in particle number is obtained shows that the iterative procedure takes advantage of the progressive reduction in the imaged seeding density of the *residual images* to recover previously untracked particles. On the other hand, more triangulations and shaking iterations could have a positive impact on the particle position accuracy. The aid of synthetic data where the ground truth is known might be necessary to assess this effect; this investigation goes beyond the scope of the present study.

The comparison of different recordings along the acquired sequence shows that the final number of tracked particles varies significantly. Figure 8b shows the imaged seeding density ( $ppp$ , blue line) along a sequence of around 300 time instants; the  $ppp$  is estimated here identifying

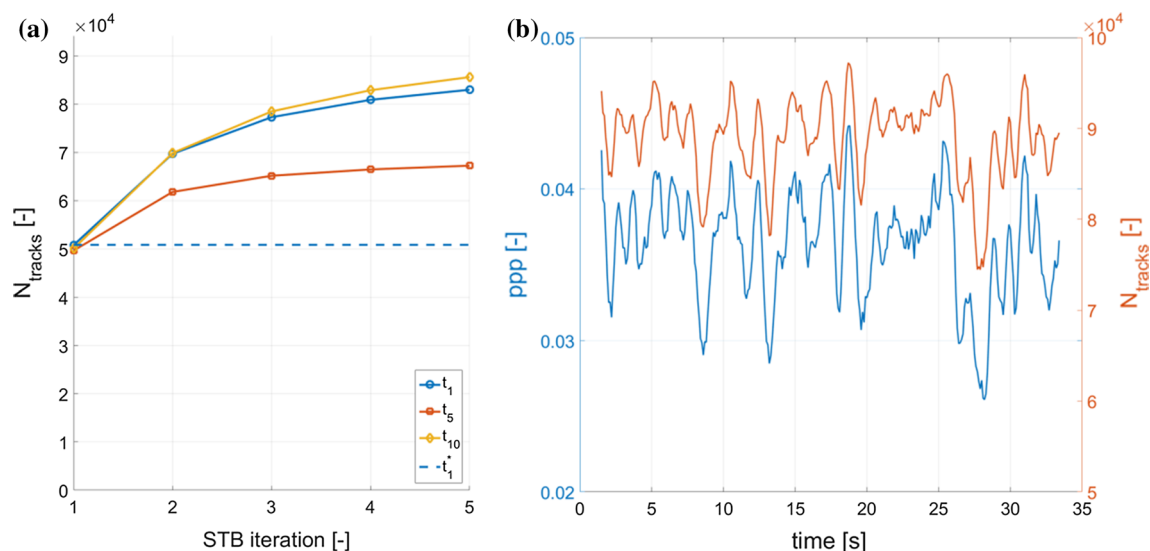


**Fig. 8** **a** Number of tracked particles at each STB iteration for three different recordings ( $t_1$ ,  $t_5$ ,  $t_{10}$ ). *Dashed line* indicates the result of a single STB iteration performed increasing the number of triangula-

tion and *shaking* iterations during IPR for recording  $t_1$  ( $t_1^*$ ). **b** Number of tracks (*orange*) and estimated imaged seeding density (*ppp*, *blue*) along approximately 300 recordings

particle peaks on a portion of the recorded image using an intensity threshold similar to that used in the STB triangulation steps ( $T_{\text{int}}$ ). The number of tracked particles after five STB iterations is shown by the orange line; the two curves show good correlation indicating that the different number of particles attained by STB corresponds to actual variations of the seeding conditions.

When considering the average  $ppp$  over the recording sequence (approximately 0.035), being the size of the active sensor around  $1600 \times 2000$  px, the estimated average number of true particles in the volume is 110,000. Results in Fig. 8 show that on average approximately 90,000 tracks are found, which suggest that around 18 % of actual particles are not tracked by STB. The loss of particle images can be ascribed to loss of polarization and Mie scattering properties resulting in a strong intensity drop of the peak intensity for one of the imaging systems but not for the other. Moreover, the fact that, in some cases, the number of STB passes employed could be not sufficient to reach a converged condition, Fig. 8a, can contribute to the lower number of attained tracks.

In Fig. 9a, a portion of the recorded image from camera 3 is shown ( $I_{\text{orig}}$ ). The *projected image* evaluated after five STB iterations shows good agreement with the original recording confirming that most true particles have been reconstructed, Fig. 9b. However, the *residual image*, Fig. 9c, shows intensity peaks that can be ascribed both to discrepancy between the calibrated OTF and the real particle shape and to actual particles that were not found by the tracking system.

The presence of the latter is confirmed when the *all-particles residual image*  $\bar{I}_{\text{res}}$  is inspected, Fig. 9d. This image

is obtained subtracting to the recorded image not only the tracked particles, but all triangulated particles as reconstructed by IPR; the lower residual intensity in  $\bar{I}_{\text{res}}$  suggests that true particles triangulated by IPR for one system are not found in the images illuminated with the other polarization direction and therefore cannot be tracked along the complete sequence of pulses. As a result, they contribute to the residual image intensity observed in  $I_{\text{res}}$ .

The computational time needed to perform one STB iteration over the four-pulse sequence is approximately 4 min (around 90,000 particle tracks in a  $50 \times 90 \times 8$  mm<sup>3</sup> volume) on a twenty cores server with two Xeon E5-2680 quad core CPUs (64 GB Ram).

A reduction in the computational burden can be achieved when full IPR is used only for the first two pulses, while the third and fourth pulse are obtained by particle prediction/correction (*shaking*) approach; since pulse  $t_1$  and  $t_2$  belong to different polarizations, the prediction step is expected not to produce ghost particles. For sake of robustness, the prediction approach is not followed here, and full IPR is performed for each pulse.

Instantaneous STB results are presented in Fig. 10. A second-order polynomial is used to fit the particles position along  $X$ ,  $Y$  and  $Z$  over the track length; a maximum threshold of 1 px for the average distance between the particles and the fit is used to reject noisy tracks ( $\sim 3$  % of the total number of tracks).

Based on analysis of synthetic images (Wieneke 2013), the position error of the reconstructed particles peak location is around 0.1 px; assuming that a second-order polynomial adequately describes the dynamics of the particle

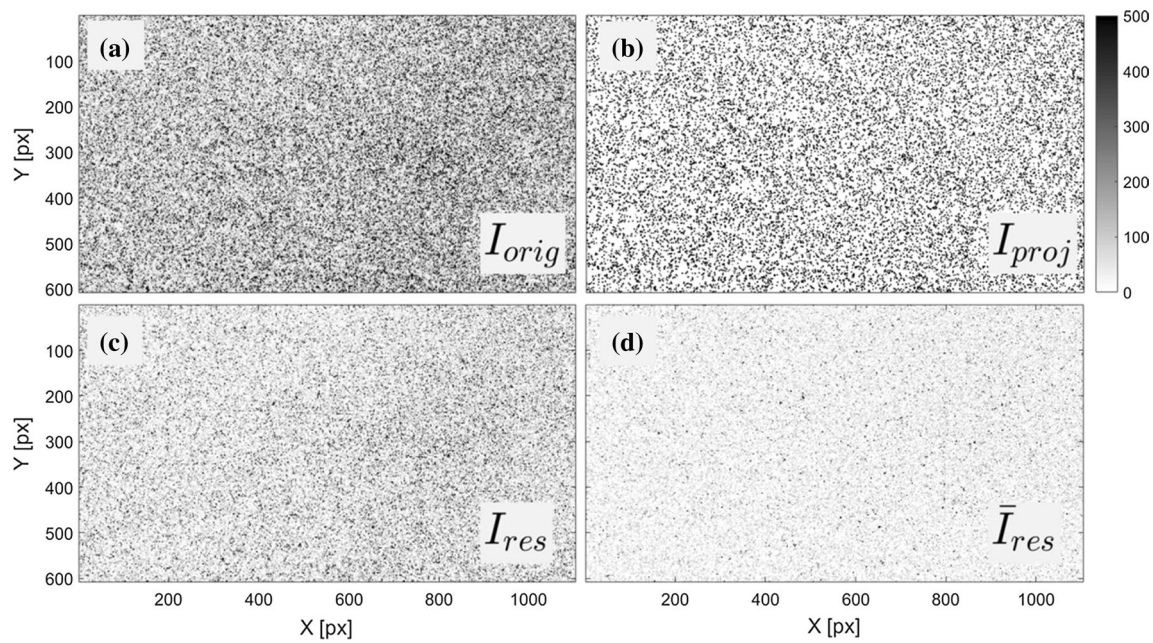


**Fig. 9** **a** Portion of original recorded image from camera 3 (inverted gray scale). **b** Projected image (5 STB iterations). **c** Residual image (only tracked particles). **d** Residual image (all triangulated particles)

tracks within the observation time, the root-mean-square error on velocity can be derived from the estimated position error as approximately 0.2 m/s. However, this value underestimates the error as it does not account for signal modulation due to sampling and for discrepancy between the polynomial function used to model the particle tracks and the real particle dynamics.

An outlier detection and removal procedure similar to what proposed by Schanz et al. (2016) is applied after the last STB iteration. For each tracked particle, the average and root-mean-square velocity values are computed within the 20 closest neighboring tracks; if the particle velocity difference with respect to the average velocity value exceeds five times the *rms* value the particle is considered as an outlier and discarded. The validation is performed after the tracks have been corrected compensating for the structural vibrations; a detailed description of the vibration shift detection and correction is found in the following section. The number of rejected outlier tracks is approximately 2 %.

Given the relatively high seeding density achieved in the present investigation, the choice of a topological neighborhood for the track validation appears to be suitable to identify outliers. On the other hand, a metric approach where all tracks within a certain distance from the considered track are included in the neighborhood could also be a viable approach. In the latter case, the size of the neighboring area can be chosen based on a physical scale relative to the

flow (e.g., the Kolmogorov scale); this strategy is not investigated in the current study.

Figure 10a, b shows the final accepted tracks (~80,000). Tracks are visualized plotting for each particle along the four pulses a spherical marker color-coded by means of the stream-wise velocity component, where both particle location and velocity are obtained from the second-order polynomial fit of the reconstructed tracks.

The particle tracks provide the velocity information on scattered data points; in order to visualize the flow features, an interpolation to regular grid is shown in Fig. 10c, d for the same time instants.

The interpolation method (FlowFit, Gesemann 2016) is based on approximating the flow field by means of a system of smooth 3D-weighted cubic b-splines, where a penalization of divergence is carried out during the evaluation of the weights in the case of incompressible flow. Spatial derivatives can be evaluated analytically from the system of b-splines.

For the result shown in Fig. 10c, d, the chosen grid spacing is 0.2 mm along the three spatial directions. The result shows that the measurement data point density achieved by the STB (approximately two tracks per cubic millimeter) is sufficient to obtain dense velocity fields suitable for the evaluation of spatial gradients. Iso-surfaces of vorticity magnitude (70001/s) are presented here to highlight the vortical structures within the turbulent boundary layer flow.



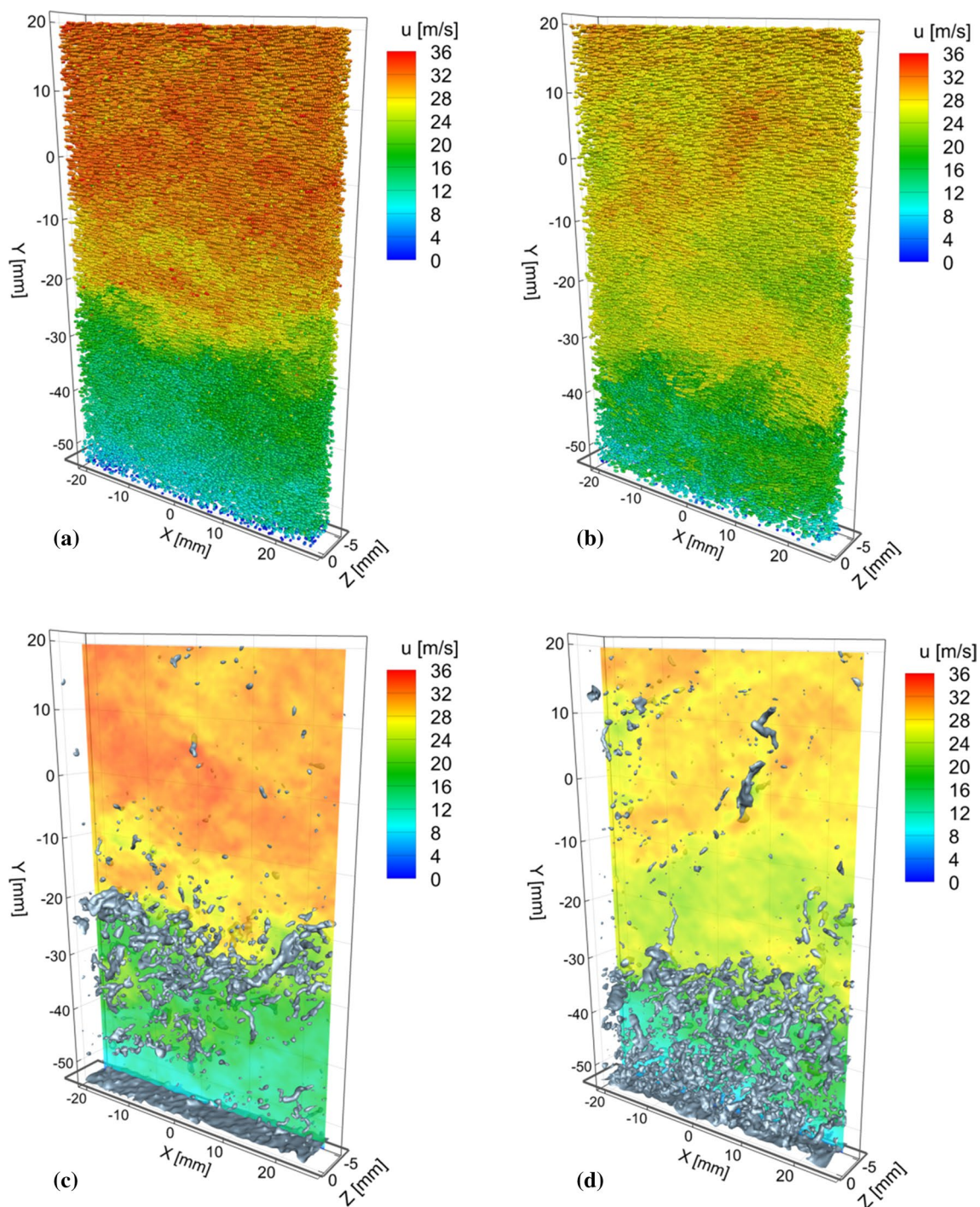


**Fig. 10** Instantaneous STB results for two different time instants (*left and right*, respectively). *Gray bold line* indicates the location of the wall surface. **a, b** Particle locations along the four-pulse tracks colored by stream-wise velocity. **c, d** FlowFit interpolation on regular

grid. Contours of stream-wise velocity component on regular grid at  $Z = -3 \text{ mm}$ ; isosurface of vorticity magnitude ( $|\omega| = 7000 \text{ 1/s}$ ) in gray

### 5.1 Vibration correction method

The calibration of the tomographic systems is carried out by imaging a 3D target with a known distribution

of markers. Volume self-calibration (Wieneke 2008) is applied to compensate for calibration errors; as this approach is based on particle images, a dedicated run at low seeding density ( $ppp \sim 0.02$ ) is recorded, where



no time separation is set between the two systems realizations.

A further self-calibration correction is performed based on the actual measurement images. As the two systems observe different particle fields it is not possible to perform a common correction; instead, two separate disparity maps are evaluated and the result is used to correct the mapping function of each imaging system.

Disparity maps are evaluated over an ensemble of 50 recordings; errors of approximately 0.1–0.5 px are observed with respect to the self-calibration correction on the dedicated run images, Fig. 11a. The residual disparity after correction is in the order of 0.01 px.

Nevertheless, when an instantaneous disparity map is evaluated based on an instantaneous recording, Fig. 11b, de-calibration errors up to 0.1–0.15 px are observed. This residual disparity is the result of structural vibrations of the recording system; in case vibrations would result in large shifts (>0.5 px), instantaneous volume self-calibration Michaelis et al. (2011) would be necessary to avoid particle loss during the IPR triangulation process.

Due to the lower frequency of structural vibrations (typically <10 Hz) when compared to that of the flow,

the relative position of particles reconstructed by a single tomographic system is not affected. On the other hand, the combination of independent disparity correction for each polarization, Fig. 11a, and of structural vibrations introduces a systematic relative shift between particles reconstructed from  $S_1$  and  $S_2$ .

The shift between the two systems effectively results in an artificial acceleration of the particles along the track and needs to be compensated for. A correction scheme for multi-pulse systems operating with two polarizations is proposed by Schröder et al. (2013) making use of velocity vector fields; in the present study, this method is adapted to the case of particle tracks.

The technique relies on the fact that the particle position within the same polarization is not biased and on the assumption that the average shift due to particle acceleration within the whole domain is zero. The latter assumption holds for small time separations between the first and last pulse in the track (30  $\mu$ s in the present case). As a consequence, when a constant shift due to acceleration between particles reconstructed by  $S_1$  and  $S_2$  is present within the whole domain, it can be ascribed to the systematic shift induced by vibrations. The correction method is designed

**Fig. 11** **a** Detail of volume self-calibration disparity maps (relative to camera 1 and camera 2 for  $S_1$  and  $S_2$ , respectively; Z plane located at  $-1$  mm, average over 50 time instants) for the two tomographic systems ( $S_1$  orange,  $S_2$  blue, reference vector—1 px—in black); disparity between run images and dedicated self-calibration images common to the two polarizations. **b** Example of two instantaneous residual disparity maps for  $S_2$

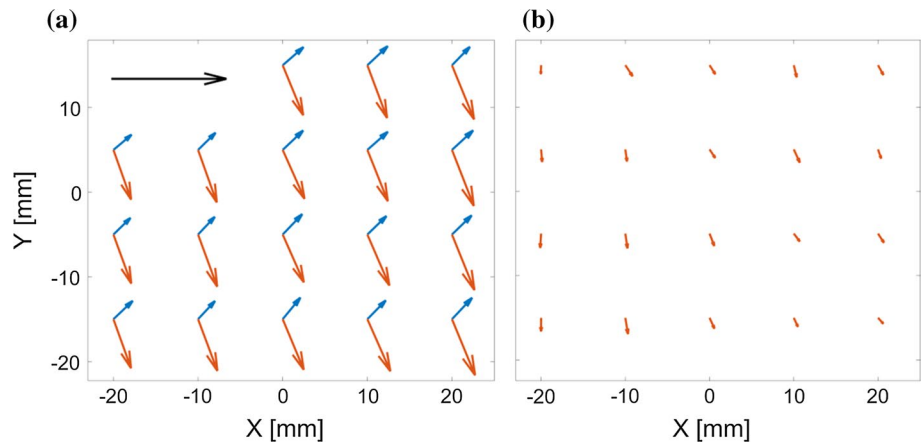
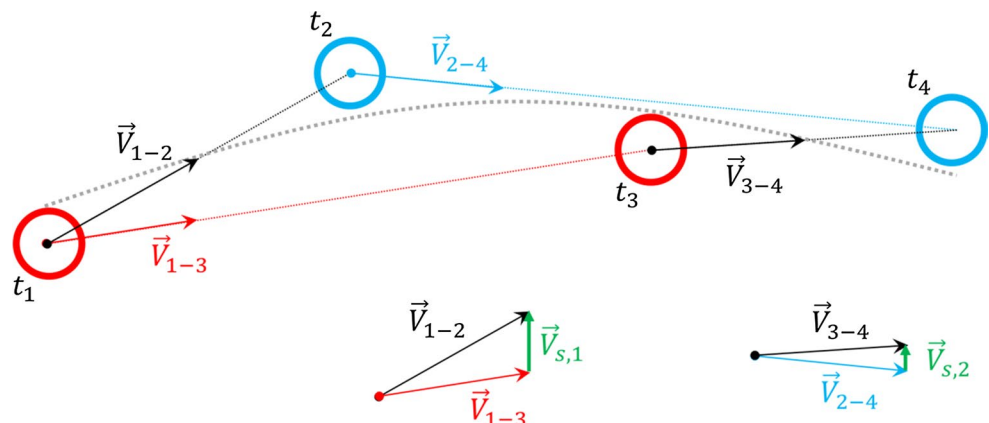


**Fig. 12** Sketch of the method used to identify the relative shift of particles between the two polarizations due to vibrations. Gray line indicates the ideal track; particles from the two systems in red and blue, respectively



to identify the shift for each instantaneous recording; a few thousand instantaneous tracks are sufficient to achieve statistical convergence.

Figure 12 shows a sketch of the shift identification procedure; a single actual track is shown in gray, and the particles from the two polarizations are shown in red and blue. A shift has been imposed displacing the two groups of particles along the vertical direction, simulating the effect of an independent displacement of the two imaging systems.

For each track  $k$ , the velocity vectors  $\vec{V}_{1-3}^k$  and  $\vec{V}_{2-4}^k$  are evaluated from the position of particles belong to the same system. Moreover, the velocity vectors from subsequent pulses are computed ( $\vec{V}_{1-2}^k$  and  $\vec{V}_{3-4}^k$ ); these can be combined to obtain  $\vec{V}_{s,1}^k$  and  $\vec{V}_{s,2}^k$  as:

$$\begin{aligned} \vec{V}_{s,1}^k &= \vec{V}_{1-2}^k - \vec{V}_{1-3}^k \\ \vec{V}_{s,2}^k &= \vec{V}_{3-4}^k - \vec{V}_{2-4}^k \end{aligned} \tag{5}$$

The *single-track-velocity shift vector*  $\vec{V}_s^k$  is obtained as:

$$\vec{V}_s^k = \frac{\vec{V}_{s,1}^k + \vec{V}_{s,2}^k}{2} \tag{6}$$

Multiplying this velocity by the time separation  $\Delta t$  results in the *single-track-displacement-shift vector*  $\vec{X}_s^k$  as:

$$\vec{X}_s^k = \vec{V}_s^k \cdot \Delta t \tag{7}$$

The final shift between the two polarization systems is obtained averaging over all the tracks  $K$  in the investigated volume:

$$\vec{X}_s = \frac{\sum_{k=1}^K \vec{X}_s^k}{K} \tag{8}$$

The components of the detected shift are then used to displace particles reconstructed from  $S_1$  and  $S_2$  toward each other applying a displacement equal to half of the detected shift.

An example of the effect of the vibration correction is shown in Fig. 13a; original particles locations are color-coded based on the polarization direction (red and blue), while corrected particles positions are shown in gray. Displacement vectors are shown in black and orange for the original and corrected tracks, respectively; for the sake of visualization, the corrected tracks have been shifted down along the vertical axis  $Y$ . The detected shift for this particular example is of 0.2 px along the  $X$  direction, 0.35 px along  $Y$  and 0.2 px along  $Z$ . As it can be observed from the track located in the upper part local acceleration events are preserved after the correction is applied.

When dividing the measurement volume in few subdomains, a particle track correction involving both translation and rotation effects would be possible. The feasibility of this approach depends on the number of tracks within each subdomain; for the current case, approximately 20,000 tracks per block would be available partitioning the volume into four subdomains, which would suffice concerning the statistical convergence.

The time history of the detected shifts along the three spatial directions is shown in Fig. 13b. The amplitude of the vibration is similar along  $X$ ,  $Y$  and  $Z$  and the maximum peak-to-peak value is around 0.3–0.4 px; these values are consistent with the levels of instantaneous disparity presented in Fig. 11b. Furthermore, a nonzero mean shift is observed which can be ascribed to the initial displacement introduced by the independent self-calibration correction based on the measurement images, Fig. 11b.

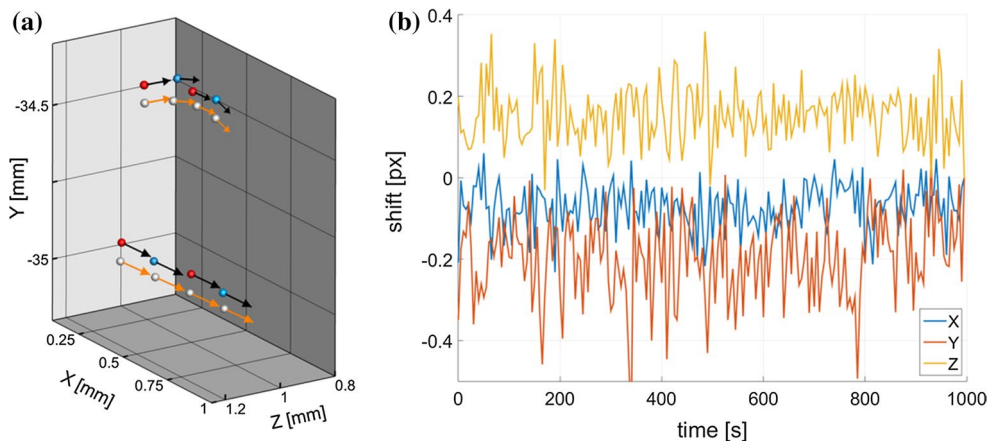


**Fig. 13** **a** Example of original (red and blue) and corrected particle locations (gray); displacement vector in black and orange, respectively. Corrected tracks are artificially shifted along the  $Y$  axis for vis-

ualization. **b** Time history of detected shifts between the two systems (one data point every 50 recordings) along  $X$ ,  $Y$  and  $Z$

## 5.2 Instantaneous wall position identification

When evaluating mean and turbulent velocity profiles in a boundary layer, the position of the wall within the measurement domain needs to be accurately determined (Cierpka et al. 2013b). A rough estimate of the wall position can be obtained during the calibration procedure, where the calibration plate is positioned close to the window surface; based on this estimate, the wall should be located at approximately  $Y_w = -54$  mm. The limited accuracy of this estimate and the presence of structural vibrations, effectively shifting the wall location within the reconstructed domain, make it necessary to implement a more accurate wall-detection method.

Looking at the recorded images, it has been observed that some particles (possibly both tracers and impurities) impact and accumulate on the glass window surface; *wall particles* are undesirable as stationary spots on the glass surface block the cameras lines-of-sight leading to loss of information on the particles in the background. For this reason, before each measurement, the glass window was carefully cleaned.

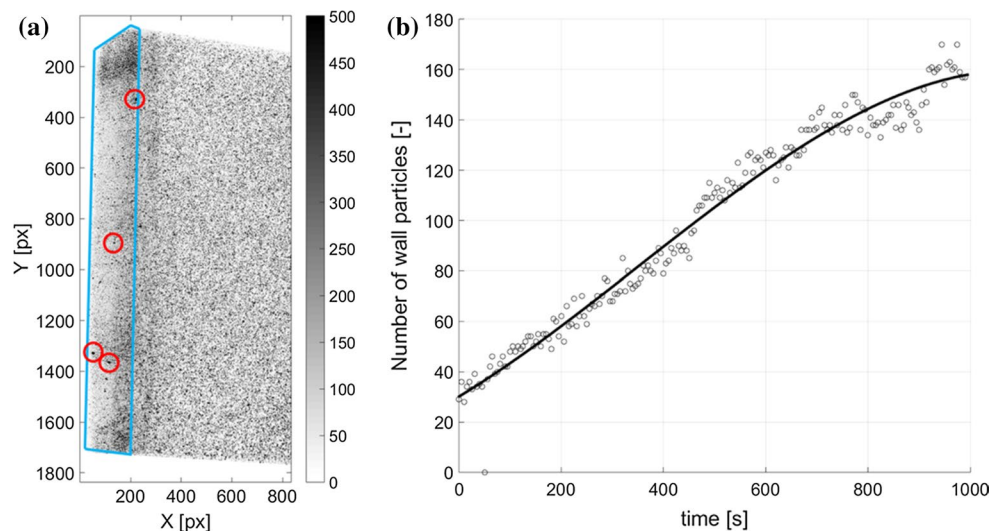
Nevertheless, some *wall particle* always appears in each recording, their number increasing over the measurement time. Since these particles are located exactly at the model surface, they can be used to accurately estimate the wall position for each instantaneous recording. A triangulation approach analogous to that employed during IPR is performed, where only the portion of the image encompassing the wall is considered, Fig. 14a. Furthermore, a high-intensity threshold ( $\approx 2500$  counts) is set for particle peaks detection, which increases the possibility to triangulate only particles at the wall; when tracer droplets impinge against the wall a large spot is produced which results in higher intensity on the image, Fig. 14a.

The optical transfer function of the *wall particles* is different from the one obtained from the particle images during the volume self-calibration; as a consequence, the accuracy of the wall particle triangulation is expected to be lower than the one of the particle tracers. Since *wall particles* do not move between the two subsequent exposures from one tomographic system, the average distance between the same triangulated particles in the first and second frame gives an indication of the triangulation accuracy (approximately  $0.15$  px  $\approx 4$   $\mu$ m—for the present case). Figure 14b shows the number of detected *wall particles* during the measurement time.

A set of *wall particles* can be found for each of the tomographic system. Ideally, the same particles should be found by  $S_1$  and  $S_2$ ; in practice, different scattering properties of the wall particle spots can result in loss of polarization, leading to different particles for the two systems. As for the particle tracers, the position of the *wall particles* from  $S_1$  and  $S_2$  can be corrected for vibrations. The effect of the vibration correction can be quantified looking at the distance between particles that are found from both systems. The average distance is reduced from approximately  $0.4$ – $0.5$  px to  $0.25$ – $0.3$  px after the vibration correction is performed. The magnitude of the residual distance between the two systems can be ascribed to the accuracy of the wall particle positioning ( $\approx 0.15$  px).

After correction, an outlier detection procedure similar to that commonly used for PIV vectors validation (Duncan et al. 2010) is applied based on the particle position along the  $Y$  axis (as the wall is expected to be approximately parallel to the  $XZ$  plane) to exclude particles which do not belong to the wall region (e.g., spurious peaks created by the laser reflections from glass imperfections). Typically, 3–5 % of the total number of particles is rejected; the values shown in Fig. 14b refer to accepted particles.

**Fig. 14** **a** Portion of image from camera 2; *blue line* highlights the wall region; examples of potential wall particles within the *red circles*. **b** Number of triangulated wall particles over 10,000 recordings (one point every 50 recordings); *curve* refers to a third-order polynomial fit



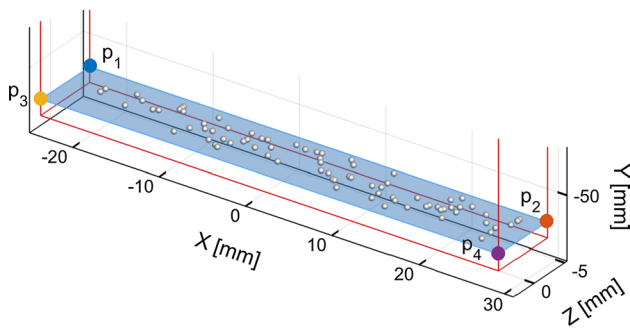
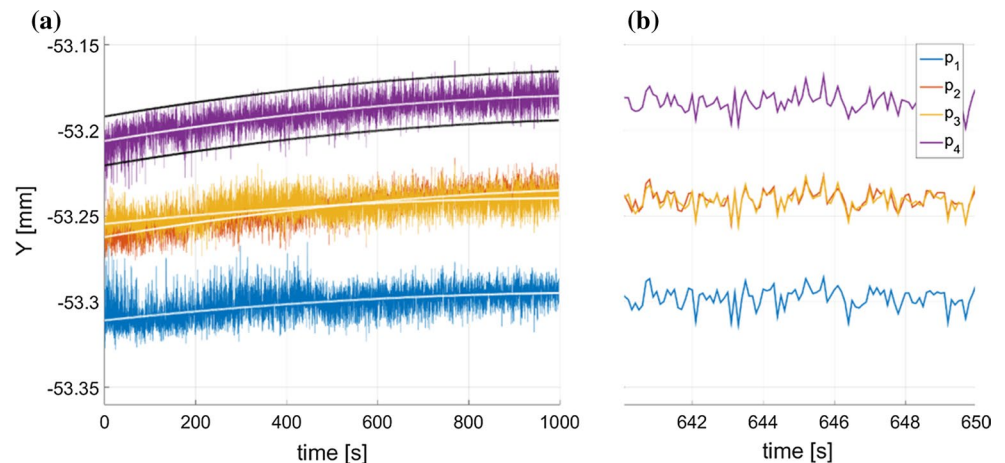


**Fig. 15** Portion of investigated domain in the wall region; domain edges in red, wall in blue, wall particles markers in gray,  $p_1, p_2, p_3, p_4$  mark the corners of the wall plane

Subsequently, the wall particle locations are used to fit a 2D plane in space which describes the surface of the glass window. The accuracy of the wall positioning depends mainly on the location accuracy of the single wall particle and on the number of particles available for the fit. Results from a Monte Carlo simulation of the plane fit show that, with the estimated accuracy of the wall particles peak location and a number of wall particles ranging from 30 to 160, as in Fig. 14b, the accuracy of the wall location is approximately 0.08 px, corresponding to 2.3  $\mu\text{m}$ . An instantaneous example of the wall plane identified by the wall particles fit is shown in Fig. 15.

The  $Y$  position of the four points located at the intersection between the edges of the investigated domain and the wall plane is shown versus the measurement time in Fig. 16; for each point, a second-order polynomial fit is shown (white curves). For  $p_4$ , the fitted curve is translated of  $\pm 0.5$  px to produce the two black curves; oscillations in the order of 1 px are observed along the time sequence which can be ascribed to the vibration of the wind tunnel structure.

**Fig. 16** **a** Time history of the  $Y$  position of the corner points of the wall ( $p_1, p_2, p_3, p_4$ , see Fig. 15) along 10,000 recordings; white line obtained with a second order polynomial fit, black lines are obtained by shifting the fit for  $p_4$  by  $\pm 0.5$  px. **b** Detailed area of approximately 10 s.



### 5.3 Boundary layer profiles and comparison with 2D techniques

Boundary layer profiles are obtained by means of ensemble averaging of the track data (Kasagi and Nishino 1990); the stream-wise location for the evaluation of the profiles ( $X = 0$  mm) is chosen such as results from 2D-PIV and long-range micro-PTV are available for comparison. Velocity components are indicated following Reynolds decomposition as  $U = \bar{U} + u$ , where  $U$  indicates the instantaneous velocity,  $\bar{U}$  the mean value and  $u$  the fluctuation; the same applies for the wall-normal ( $V$ ) and span-wise ( $W$ ) components.

Velocity is evaluated at the midpoint of each track from the polynomial fit, and results are collected into two-dimensional bins encompassing 10 mm in stream-wise ( $X$ ) direction and 0.04 mm along the wall-normal direction ( $Y$ ); bins extend over the entire volume span ( $Z$ ). A sequence of 10,000 recordings is analyzed resulting in approximately 30,000 samples within each bin.

For the PIV and micro-PTV results, 20,000 and 30,000 recordings are analyzed, respectively. For the large-scale PIV measurements, all acquired images are evaluated using window correlation with final interrogation sizes of  $16 \times 16$  px and an overlap of 50 %. A two-frame probabilistic approach is applied for the micro-PTV. As for the 3D tracking evaluation, averaging is performed over two-dimensional bin extending 10 mm in stream-wise and 0.008 mm ( $0.4l^+$ ) in the wall-normal direction. Further details regarding the PIV and micro-PTV results can be found in Reuther et al. (2015).

The friction velocity  $u_\tau = 0.78$  is estimated by means of the Clauser chart method from long-range micro-PTV results (Reuther et al. 2015). Given the kinematic viscosity  $\nu = 1.54 \times 10^{-5} \text{ m}^2/\text{s}$ , a viscous length ( $l^+$ ) of 0.02 mm is



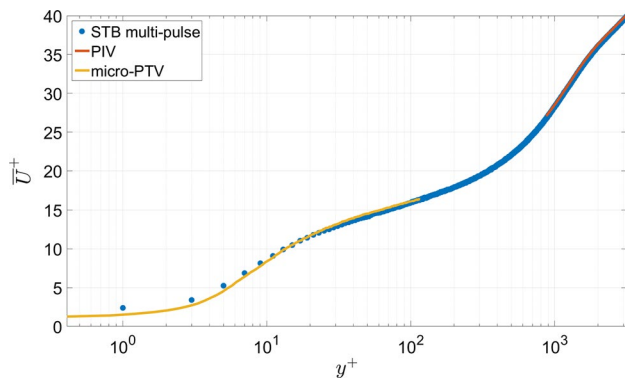


**Fig. 17** Mean normalized stream-wise velocity component from 2D-PIV, long-range micro-PTV and 3D STB multi-pulse particle tracking

estimated. The wall-normal coordinate and the velocity are expressed in wall units as:

$$y^+ = \frac{y \cdot u_\tau}{\nu} \tag{9}$$

$$U^+ = \frac{U}{u_\tau}$$

The bin size along the wall-normal direction equals two wall units. An average wall location is considered for the following results ( $Y_w = -53.24$  mm).

Profiles relative to the mean stream-wise velocity component are shown in Fig. 17. These results show that the multi-pulse particle tracking-based technique is able to deliver accurate results over a wide range of spatial scales. Good agreement between the results from the different techniques is observed for  $y^+ > 10$ . It can be observed that the cross-correlation-based technique suffers from the limitations in terms of spatial resolution posed by the finite size of the interrogation region; as a consequence, PIV results can be considered reliable for  $y^+ > 900$ . Conversely, when a high magnification approach is used (long-range micro-PTV) a relatively small field of view can be investigated (approximately 20 mm<sup>2</sup>), which limits the observation to the near-wall region ( $y^+ < 100$ ).

The macroscopic field of view of the multi-pulse approach (50 × 90 × 8 mm<sup>3</sup>) covers both the aforementioned investigated areas and fills the gap region between  $y^+ = 100$  and  $y^+ = 900$  left by the 2D techniques.

The fact that a single measurement technique can be used to simultaneously investigate the near-wall region as well as the outer region of the turbulent boundary represents an advantage in terms of the range of scales that can be resolved. The temporal information exploited by the STB technique makes large field high-resolution measurements possible.

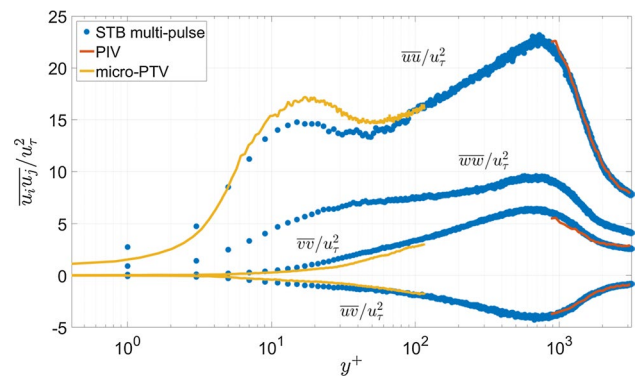


**Fig. 18** Profiles of Reynolds stress fluctuations from 2D-PIV, long-range micro-PTV and 3D STB multi-pulse particle tracking

Furthermore, the instantaneous measurement of the complete velocity vector and gradient tensor components offers the possibility to characterize the flow structures (e.g., two-point correlation approaches).

While the profiles shown in Fig. 17 overlap within the outer region of the boundary layer, larger differences can be observed in the near-wall region, particularly regarding the fluctuating velocity components for  $y^+ \leq 50$  (Fig. 18). However, both the micro-PTV and STB multi-pulse approach nicely resolve the inner peak of the stream-wise turbulence intensity located at  $y^+ \sim 15$ .

In the near-wall region, the small particle displacement between two subsequent recordings results in a larger relative error for both the STB and micro-PTV methods. On the other hand, the fact that a higher mean velocity is found for  $y^+ < 10$  for the STB suggests the presence of a bias error. This hypothesis is corroborated by the visual inspection of the camera images; the laser light impinging on the glass surface of the window providing optical access to the test section results in significant reflections and glare on the images, Fig. 14a.

Despite the application of image pre-processing techniques (i.e., minimum image subtraction), these reflections cannot be completely removed and result in the formation of spurious particle tracks in the near-wall region. With the aim of reducing this effect, a higher threshold for the 2D particle peak detection ( $T_{int} = 300$  counts) has been chosen to produce the results shown in Figs. 17 and 18, which results in approximately 30,000–40,000 reconstructed tracks for each instantaneous recording. Furthermore, in order to reduce the effect of potential outliers, entries exhibiting fluctuations larger than  $4 \cdot \vec{v}_{rms}$  have been excluded from the statistical analysis.

Nevertheless, results seem to indicate that this approach is not sufficient to eliminate the effects of the illumination issues. The use of high quality coated glass is therefore

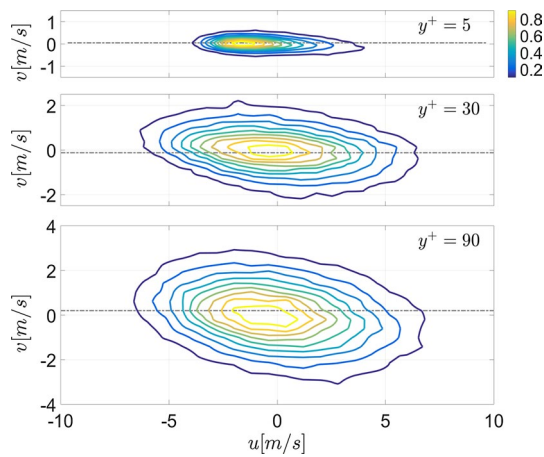


**Fig. 19** Joint PDF of stream-wise and wall-normal velocity fluctuation components two wall-normal locations;  $y^+ = 5/30/90$ . Dashed gray lines at constant  $v$  value corresponding to the location of the PDF peak value  $v_{PDF_{max}} = 0.05/-0.12/0.19$  m/s for the three  $y^+$  stations, respectively

strongly suggested when near-wall regions are of interest, particularly if the light used for the volume illumination impinges directly on the wall surface.

The joint probability density function (PDF) of the stream-wise and wall-normal velocity fluctuation components is shown at three different stations along the wall-normal direction ( $y^+ = 5/30/90$ ) at  $X = 0$  mm, Fig. 19. Results refer to an area of  $8.5 \times 0.02$  mm<sup>2</sup> along  $X$  and  $Y$  around the reference point; all entries along the span-wise direction have been included. Profiles are extracted at a constant  $v$  value corresponding to the location of the peak of the PDF distribution ( $v_{PDF_{max}}$ ); the comparison between the STB and long-range micro-PTV results is shown in Fig. 20. Results are consistent with what observed in the

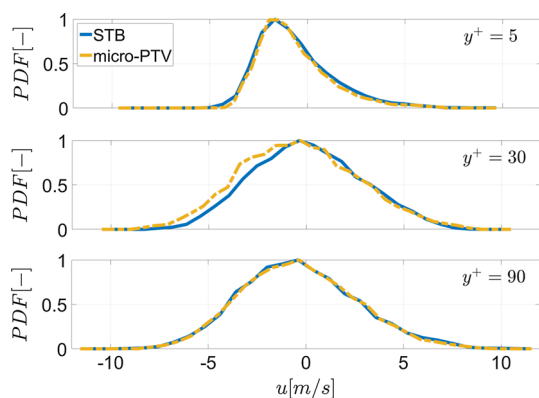


**Fig. 20** Profiles extracted across the peak of the PDF distributions ( $v = v_{PDF_{max}}$ , gray dashed lines in Fig. 19) at three wall-normal locations;  $y^+ = 5/30/90$ ; comparison between STB and long-range micro-PTV results

comparison of the Reynolds stresses profiles in Fig. 18, where the fluctuation values seem to be slightly underestimated for the STB case in proximity of  $y^+ = 30$ .

## 6 Conclusions and outlook

The main motivation for the current study is to extend the capabilities of the STB technique, initially proposed for time-resolved recordings, to short image sequences as obtained from multi-pulse illumination and imaging systems.

The use of two independent double-pulse lasers allows for the generation of four-pulse sequences, where the time delay between recordings can be reduced down to a few microseconds. As a consequence, the time evolution of particle tracers can be accurately followed by the 3D tracking algorithm at any high flow speed, where high-speed systems cannot be employed due to the current limitations in terms of illumination intensity and acquisition frequency.

The Lagrangian particle tracking approach is needed to avoid the signal modulation introduced by cross-correlation-based algorithms as a consequence of the finite size of the interrogation volumes. This situation is particularly critical when strong gradients and near-wall regions are considered as for many relevant aerodynamics applications (e.g., shear flows and boundary layers).

An iterative STB approach is proposed in the present study which makes use of the sequential application of IPR and particle tracking in order to progressively reduce the complexity of the object to be reconstructed (image seeding density). The use of two independent imaging systems, where cameras have different viewing directions with respect to the investigated domain, aids the reconstruction process as the formation of coherent ghost tracks is avoided. As a consequence, high particle seeding densities can be dealt with, making the STB multi-pulse technique suitable for offering access to both highly resolved flow statistics and instantaneous 3D flow structures.

The application of the method to four-pulse images from a turbulent boundary layer with adverse pressure gradient experiment in air is discussed. The free-stream velocity is 36 m/s and the measurement volume encompasses  $50 \times 90 \times 8$  mm<sup>3</sup> along the stream-wise, wall-normal and span-wise direction, respectively. The adopted pulse separation strategy makes use of polarized laser light following Schröder et al. 2013. Approximately 80,000 instantaneous tracks are identified for each multi-pulse recording. The achieved seeding density grants access to the complete velocity gradient tensor; scattered data from particle tracking data are interpolated on a regular grid to visualize vortical flow structures.

The discrepancy between the estimated imaged particle number and the number of instantaneous tracks identified

by STB can be addressed to loss of polarization and Mie scattering properties, potentially resulting in strong differences of particle peak intensity between the two imaging systems, eventually resulting in loss of particles across the four-pulse sequence.

A method to identify and compensate for structural vibrations resulting in camera displacement is adapted from what proposed by Schröder et al. (2013). The technique relies on the short-time separation between pulses (30  $\mu\text{s}$  between the first and last pulse) and on the number of particle tracks used for the statistical evaluation. Unsteady shifts up to approximately 0.3–0.4 px are detected, consistently with what suggested by the instantaneous self-calibration residual disparity. The detected shifts are used to correct the particles position along the tracks for each instantaneous realization.

The presence of stationary particles at the wall glass surface allows for the accurate detection of the wall position based on triangulation. The accuracy of the reconstructed wall location is estimated to be in the order of 2  $\mu\text{m}$ . As the structural vibrations result in large displacements (up to 30  $\mu\text{m}$ ) of the wall surface along the acquisition time, the instantaneous wall position can be exploited to reposition the instantaneous track fields at the correct physical location with respect to the wall.

An ensemble averaging approach is followed to evaluate highly spatially resolved turbulent boundary layer profiles, where the bin size along the wall-normal direction is reduced to  $2l^+$  (0.02 mm). Mean and fluctuating velocity profiles and joint probability density function of the stream-wise and wall-normal fluctuating velocity components are compared to results from 2D-PIV and long-range micro-PTV (Reuther et al. 2015).

Results show good agreement along a wide range of spatial scales and confirm the potential of the 3D particle tracking-based multi-pulse technique in providing accurate results suitable both to the evaluation of instantaneous velocity spatial gradients and high-resolution statistics, where the near-wall and outer region of the flow can be investigated employing a single measurement technique. Differences between the different experimental techniques observed in the near-wall region ( $y^+ < 30$ ) suggest the presence of outliers introduced as a consequence of imperfection in the glass surface granting optical access to the imaging system; the use of high quality coated glass is advised for future investigations.

A dedicated investigation of the STB performances based on synthetic multi-pulse data has been recently presented by Novara et al. (2016), where the availability of the ground truth velocity and acceleration distributions allows for the quantitative assessment of the effect of experimental and processing parameters on the accuracy of the STB results. In particular, the choice of

an uneven distribution of the pulses in time in order to increase the measurement dynamic range is investigated, eventually allowing for the measurement of the material acceleration and potentially of the instantaneous pressure field, the latter being of particular interest for industrial applications.

An alternative strategy for pulse separation based on the use of frame-optimized exposure cameras remains to be investigated, which potentially allows avoiding imaging issues related to the use of polarized light.

**Acknowledgments** This work has been conducted in the framework of the DFG-project “Analyse turbulenter Grenzschichten mit Druckgradient bei großen Reynoldszahlen mit hochauflösenden Vielkammermessverfahren” (Grant KA 1808/14-1 and SCHR 1165/3-1).

## References

- Atkinson C, Soria J (2009) An efficient simultaneous reconstruction technique for tomographic particle image velocimetry. *Exp Fluids* 47:563–578
- Ben Salah R, Alata O, Tremblais B, Thomas L, David L (2015) Particle Volume Reconstruction based on a marked point process and application to Tomo-PIV. 23rd European Signal Processing Conference
- Cierpka C, Lütke B, Kähler CJ (2013a) Higher order multi-frame particle tracking velocimetry. *Exp Fluids* 54:1533–1545
- Cierpka C, Scharnowski S, Kähler CJ (2013b) Parallax correction for precise near-wall flow investigations using particle imaging. *Appl Opt* 52:2923–2931
- Cornic P, Champagnat F, Cheminet A, Leclaire B, Le Besnerais G (2013) Computationally efficient sparse algorithms for tomographic PIV reconstruction. In: 10th symposium PIV Delft, The Netherlands
- Cornic P, Champagnat F, Plyer A, Leclaire B, Cheminet A, Le Besnerais G (2014) Tomo-PTV with sparse tomographic reconstruction and optical flow. In: 17th international symposium on application of laser techniques to fluid mechanics, Lisbon, Portugal, 7–10 July
- Discetti S, Ianiro A, Astarita T, Cardone G (2013) On a novel low cost high accuracy experimental setup for tomographic particle image velocimetry. *Meas Sci Technol* 24:075302
- Duncan J, Dabiri D, Hove J, Gharib M (2010) Universal outlier detection for particle image velocimetry (PIV) and particle tracking velocimetry (PTV) data. *Meas Sci Technol* 21:057002
- Elsinga GE, Tokgoz S (2014) Ghost hunting—an assessment of ghost particle detection and removal methods for tomographic-PIV. *Meas Sci Technol* 24:035305
- Elsinga GE, Scarano F, Wieneke B, van Oudheusden BW (2006) Tomographic particle image velocimetry. *Exp Fluids* 41:933–947
- Elsinga GE, Westerweel J, Scarano F, Novara M (2011) On the velocity of ghost particles and the bias error in tomographic-PIV. *Exp Fluids* 50:825–838
- Geisler R (2014) A fast double shutter system for CCD image sensors. *Meas Sci Technol* 25:025404
- Gesemann S (2016) From particle tracks to velocity and acceleration fields using B-splines and penalties. [arXiv:1510.09034](https://arxiv.org/abs/1510.09034)
- Herman GT, Lent A (1976) Iterative reconstruction algorithms. *Comput Biol Med* 6:273–294
- Huhn F, Schanz D, Gesemann S, Schröder A (2015) Pressure fields from high-resolution time-resolved particle tracking velocimetry

- in 3D turbulent flows. In: Proceedings of NIM2015 workshop, Poitiers, France
- Kähler CJ, Kompenhans J (2000) Fundamentals of multiple plane stereo particle image velocimetry. *Exp Fluids* 29:S70–S77
- Kähler CJ, Scholz U, Ortmanns J (2006) Wall-shear-stress and near-wall turbulence measurements up to single pixel resolution by mean of long-distance micro-PIV. *Exp Fluids* 41:327–341
- Kähler CJ, Scharnowski S, Cierpka C (2012a) On the resolution limit of digital PIV. *Exp Fluids* 52:1629–1639
- Kähler CJ, Scharnowski S, Cierpka C (2012b) On the uncertainty of digital PIV and PTV near walls. *Exp Fluids* 52:1641–1656
- Kasagi N, Nishino K (1990) Probing turbulence with three-dimensional particle tracking velocimetry. *Exp Therm Fluid Sci* 4:601–612
- Lynch KP, Scarano F (2013) A high-order time-accurate interrogation method for time-resolved PIV. *Meas Sci Technol* 24:035305
- Lynch KP, Scarano F (2014) Material acceleration estimation by four-pulse tomo-PIV. *Meas Sci Technol* 25:084005
- Lynch KP, Scarano F (2015) An efficient and accurate approach to MTE-MART for time-resolved tomographic PIV. *Exp Fluids* 56:66
- Maas HG, Gruen A, Papantoniou D (1993) Particle tracking velocimetry in three dimensional flows. *Exp Fluids* 15:133–146
- Michaelis D, Wolf C (2011) Vibration compensation for tomographic PIV using single image volume self-calibration. In: 9th international symposium of PIV, Kobe, Japan
- Novara M, Batenburg KJ, Scarano F (2010) Motion tracking-enhanced MART for tomographic PIV. *Meas Sci Technol* 21:035401
- Novara M, Ianiro A, Scarano F (2013) Adaptive interrogation for 3D-PIV. *Meas Sci Technol* 24:024012
- Novara M, Schanz D, Gesemann S, Lynch K, Schröder A (2016) Lagrangian 3D particle tracking for multi-pulse systems: performance assessment and application of Shake-The-Box. In: 18th international symposium on application of laser techniques to fluid mechanics, Lisbon, Portugal, 4–7 July
- Reuther N, Schanz D, Scharnowski S, Hain R, Schröder A, Kähler CJ (2015) Experimental investigation of adverse pressure gradient turbulent boundary layers by means of large-scale PIV. In: 11th symposium PIV, Santa Barbara, CA, USA
- Schanz D, Gesemann S, Schröder A, Wieneke B, Novara M (2013a) Non-uniform optical transfer function in particle imaging: calibration and application to tomographic reconstruction. *Meas Sci Technol* 24:024009
- Schanz D, Schröder A, Gesemann S, Michaelis D, Wieneke B (2013b) Shake-the-Box: a highly efficient and accurate tomographic particle tracking velocimetry (TOMO-PTV) method using prediction of particle position. In: 10th symposium PIV, Delft, The Netherlands
- Schanz D, Gesemann S, Schröder A (2016) Shake-The-Box: Lagrangian particle tracking at high particle image densities. *Exp Fluids* 57:70
- Scharnowski S, Kähler CJ (2013) On the effect of curved streamlines on the accuracy of PIV vector fields. *Exp Fluids* 54:1435
- Schröder A, Schanz D, Geisler R, Willert C, Michaelis D (2013) Dual-volume and four-pulse tomo-PIV using polarized light. In: 10th symposium PIV, Delft, The Netherlands
- Schröder A, Schanz D, Michaelis D, Cierpka C, Scharnowski S, Kähler CJ (2015) Advances of PIV and 4D-PTV Shake-The-Box for turbulent flow analysis—the flow over periodic hills. *Flow Turbul Combust*. doi:10.1007/s10494-015-9616-2
- Theunissen R, Scarano F, Riethmuller ML (2008) On the improvement of PIV image interrogation near stationary interfaces. *Exp Fluids* 45:557–572
- Van Oudheusden BW (2013) PIV-based pressure measurement. *Meas Sci Technol* 24:032001
- Wieneke B (2008) Volume self-calibration for 3D particle image velocimetry. *Exp Fluids* 45:549–556
- Wieneke B (2013) Iterative reconstruction of volumetric particle distribution. *Meas Sci Technol* 24:024008